

Central East Pacific Flight Routing

Shon Grabbe* and Banavar Sridhar†

NASA Ames Research Center, Moffett Field, CA, 94035-1000

Nadia Cheng‡

University of California—San Diego, La Jolla, CA, 92093-0411

This paper examines the potential benefits of transitioning from the fixed Central East Pacific routes to user-preferred routes. A minimum-travel-time, wind-optimal dynamic programming algorithm was developed and utilized as a surrogate for the actual user-provided routing requests. After first describing the characteristics of the flights utilizing the Central East Pacific routes for a five-day period, the results of both nominal and wind-optimal routing simulations are presented. The average potential time and distance savings for the wind-optimal routes was 9.9 min and 36 nmi per flight, respectively. When the wind-optimal routing flight plan deviations were confined within the oceanic center boundary, the average potential time and distance savings were 4.8 min and 4.0 nmi per flight, respectively. These results are likely an upper bound on the potential savings due to the location of the polar jet stream during this five-day period. Although the sector loading did not significantly change under the wind-optimal routing simulations, the number of simulated first-loss-of-separation events did, which could contribute to increased controller workload.

I. Introduction

The Oakland Oceanic Flight Information Region (FIR) (or Center), which is shown in Fig. 1, controls approximately 21.3 million square miles of airspace and borders the Anchorage FIR to the north, the Tokyo FIR to the west, the Auckland FIR to the south, and the coastline of the contiguous United States on the east.¹ In contrast, the twenty Air Route Traffic Control Centers (ARTCCs) in the contiguous U.S. encompass roughly 3 million square miles. Despite the vast amount of airspace controlled by Oakland Center, flights, for the most part, are required to fly along fixed route structures and adhere to lateral separation standards that extend up to 100 nmi, longitudinal separation standards extending up to 15 min, and vertical separation standards of 1000 ft.² These stringent separation standards are required because of the limited surveillance capabilities in the ocean and the FAA's legacy Oceanic Display and Planning System (ODAPS).

With the introduction of the FAA's new Advanced Technologies & Oceanic Procedures (ATOP) at Oakland Center in 2005, increased route flexibility and reduced separation standards can potentially be accommodated. Some of the major ATOP innovations leading to this increased flexibility are (1) fully integrated flight- and radar-data-processing capabilities, (2) conflict-detection capabilities, and (3) satellite data-link communication and surveillance capabilities.³ This paper presents the results of a study examining the potential benefits and consequences of allowing user-preferred routing in place of the fixed Central East Pacific (CEP) routes.

* Research Scientist, Automation Concepts Research Branch, Mail Stop 210-10, Shon.R.Grabbe@nasa.gov.

† Chief, Automation Concepts Research Branch, Mail Stop 210-10, Fellow AIAA.

‡ Student, Dept. of Mechanical and Aerospace Engineering.

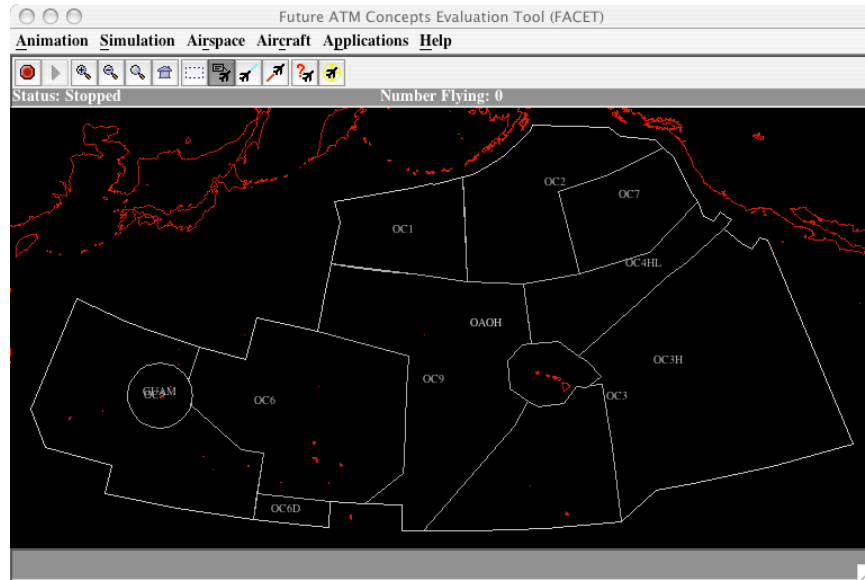


Figure 1. Oakland Oceanic Center display including sector boundaries and coastal map.

The CEP routes shown in Fig. 2 connect the west coast of the United States to Hawaii. Oakland Oceanic Sectors 3 (OC-3) and 4 (OC-4) handle traffic along these routes. Routes R464 and R576 that are shown in green are used exclusively for westbound traffic, while routes R465, R585, and R577 that are shown in magenta are used exclusively for eastbound traffic. Routes R463 and R578 that are shown in orange can accommodate bi-directional traffic. The Required Navigation Performance (RNP) for aircraft flying on the CEP routes is 10, or RNP-10, which implies that the total cross-track and along-track errors relative to the flight plan cannot exceed 10 nmi for more than 95% of the flight time.^{2,4} These flights can be identified by the “/R” equipment suffix appearing in their International Civil Aviation Organization (ICAO) flight plans.⁵ Based on the required equipage level for flights operating on the CEP routes, the lateral separation standards are 50 nmi, the longitudinal separation standards vary between 5 and 10 minutes, and the vertical separation standards are 1000 ft. The variation in the longitudinal separation standard is dependent on whether or not flights are adhering to the “Mach Number Technique.” When this technique is employed, as is commonly done on the CEP routes, the longitudinal separation standard depends on the difference between the assigned Mach number of the trailing and leading aircraft. For example, if the leading aircraft maintains a Mach number equal to that of the trailing aircraft then 10 minutes longitudinal spacing is required. However, if the leading aircraft is Mach 0.06 faster than the trailing aircraft then 5 minutes longitudinal spacing is enforced.²

It is believed that this is the first study to explore the benefits of transitioning from the fixed CEP-based route structure to a more flexible user-preferred routing structure. To date, a comprehensive investigation of the potential time savings to the airspace users, and the potential impact of user preferred routing on the air traffic service provider has not appeared in the literature. The results of this study can serve as an initial basis for considering the adoption of user preferred routing over the existing fixed routing structure in this region of the ocean. Though the flight routing application in this study is believed to be unique, the general area of flight plan routing and flight path design has a long history.⁶ Recent advances in this area include the conflict-free, wind-optimal routing work that was introduced in Ref. 7, the dynamic network flow rerouting approach introduced in Ref. 8, and the fleet assignment and routing approach introduced in Ref. 9. A comprehensive summary of many of the earliest flight routing techniques can be found in Ref. 10.

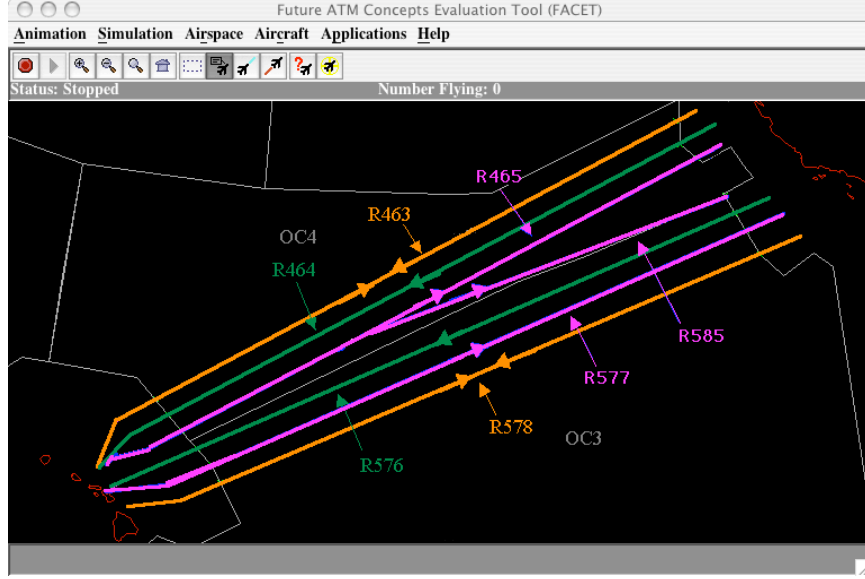


Figure 2. Central East Pacific (CEP) routes.

The rest of this paper is organized as follows. Section II describes the wind-optimal routing method that was adopted for this paper. The unmodified characteristics of the CEP routes are described in Section III and the modeling results are presented in Section IV. Finally, Section V ends with some conclusions.

II. Modeling Method

With ATOP, it is now conceivable to transition from the fixed CEP route structure in the Pacific to a set of routes that accommodate the airline user’s preferences, which are assumed to be wind-optimal for this study. To begin understanding the potential implications of this transition, a minimum-travel-time, wind-optimal dynamic programming (DP) algorithm was developed to simulate possible user route preferences. Though the business models, schedules, and aerodynamic performance characteristics of the aircraft in the airline’s fleet will ultimately govern the design of the optimal trajectories each airline wishes to fly, a simple minimum-time wind-optimal model should initially suffice to understand this change in routing philosophy. The remainder of this section is organized as follows. In Section II.A, the standard dynamic programming recursion relation will be presented, and details concerning the dynamic programming grid are presented in Section II.B.

A. Dynamic Programming Recursion Relation

The position of an aircraft along a minimum-time wind-optimal route at stage $k+1$ can be related to the position at stage k via the following equation:

$$x_{k+1} = x_k + u_k \quad (1)$$

Here u_k is the decision variable at stage k . Wind-optimal routes are then calculated on a grid composed of latitude and longitude values that encompasses the region of airspace in which each aircraft travels. Though the grid is individually tailored for each flight, it is roughly bounded between the 20° north latitude to the south, 40° north latitude to the north, 156° west longitude to the west, and 120° west longitude to the east. This grid is sufficient for most flights that either depart or arrive at the west coast of the United States. For flights departing or arriving at inland airports, such as Chicago O’Hare International Airport, the grid is increased accordingly.

Within this problem formulation, the states x_k refer to the set of latitude/longitude points, (λ_k, τ_k) that are available at stage k ; and the decision variable u_k represents the set of admissible changes in latitude and longitude that are permitted at each stage. The admissible states and decision variables that are available at each stage will be discussed in more detail in Section II.B.

Using the principle of optimality, the minimum cost function at stage k , $I(x,k)$, can be calculated from the minimum cost function at stage $k+1$, $I(x_k + u_k, k+1)$ using the following expression:¹¹

$$I(x,k) = \min_{u_k \in U_k} \{C(x_k, u_k, k) + I(x_k + u_k, k+1)\} \quad \text{for } k \in \{0, 1, \dots, N-1\} \quad (4)$$

Here $C(x_k, u_k, k)$ is the incremental cost associated with transitioning from state x_k to x_{k+1} using the decision variable u_k at stage k . For our study, the cost is equal to the amount of time required for an aircraft to fly from the current state, x_k , to the next state, x_{k+1} . The details of the cost function calculations are provided in the Appendix. The sequence of controls (i.e., u_0, u_1, \dots, u_{N-1}) resulting from the solution of Eq. 4 for $0 \leq k \leq N-1$ is used to construct the minimum-time, wind-optimal routes between the origin and destination airport for each flight. For all routes generated using Eq. 4, the minimum cost function at $k=N$ (i.e., $I(x,N)$) has been set to zero.

To illustrate the use of this algorithm, wind-optimal trajectories for the east- and westbound aircraft that were nominally flying on the CEP routes are presented in the fourth section of this paper.

B. Dynamic Programming Grid

For a given starting- and end-point, the process of generating the set of admissible states and decision variables for use in Eq. (4) involves three steps. In the first step, a series of $(N^{mid} - 2)$ intermediate, equally spaced points is generated along the great circle route connecting the starting- and end-point. If the ending point (i.e., the origin airport) is denoted by $(\lambda_0^{mid}, \tau_0^{mid})$ and the starting point (i.e., the destination airport) is denoted by $(\lambda_{N^{mid}}^{mid}, \tau_{N^{mid}}^{mid})$ then the remaining $(N^{mid} - 2)$ points are given by¹²

$$\lambda_i^{mid} = \tan^{-1}(z_i / \sqrt{x_i^2 + y_i^2}) \quad (5)$$

$$\tau_i^{mid} = \tan^{-1}(y_i / x_i) \quad (6)$$

where

$$x_i = A_i \cos \lambda_0^{mid} \cos \tau_0^{mid} + B_i \cos \lambda_{N^{mid}}^{mid} \cos \tau_{N^{mid}}^{mid} \quad (7)$$

$$y_i = A_i \cos \lambda_0^{mid} \sin \tau_0^{mid} + B_i \cos \lambda_{N^{mid}}^{mid} \sin \tau_{N^{mid}}^{mid} \quad (8)$$

$$z_i = A_i \sin \lambda_0^{mid} + B_i \sin \lambda_{N^{mid}}^{mid} \quad (9)$$

$$A_i = \sin((1 - f_i) d_{0 \rightarrow N^{mid}}^{mid} / \sin d_{0 \rightarrow N^{mid}}^{mid}) \quad (10)$$

$$B_i = \sin(f_i d_{0 \rightarrow N^{mid}}^{mid} / \sin d_{0 \rightarrow N^{mid}}^{mid}) \quad (11)$$

Here $f_i \in \{x \in \mathfrak{R} \mid 0 \leq x \leq 1\}$ is the fraction of the distance between the starting and end points at which to create a new intermediate point and $d_{0 \rightarrow N^{mid}}^{mid}$ is the great circle distance between the starting and end points that can be calculated from Eq. (16) in the Appendix. A simple example in which $N^{mid} = 4$ and $f_i = \{1/3, 2/3\}$ is shown in Fig. 3. The four blue circles in this figure represent the intermediate points.

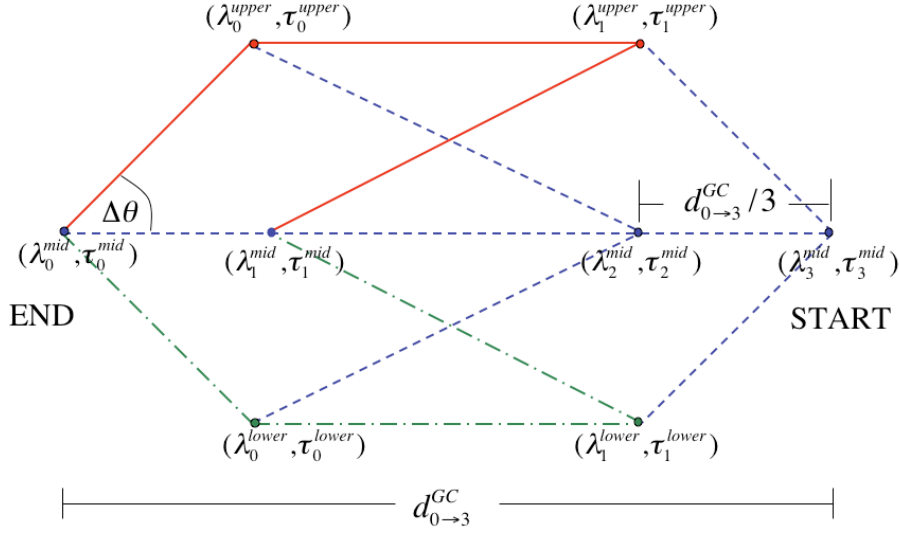


Figure 3. Sample dynamic programming grid.

The second step in creating the latitude and longitude grid entails the calculation of the upper and lower points that are depicted by the red and green circles, respectively, in Fig. 3. These offset points (i.e., the lower and upper points) are calculated using the following methodology:

$$\lambda_i^{offset} = \sin^{-1} \left[\sin \lambda_i^{mid} \cos d_{offset} + \cos \lambda_i^{mid} \sin d_{offset} \cos \phi_i \right] \quad (12)$$

$$\Delta \tau_i^{offset} = \tan^{-1} \left[\sin \phi_i \sin d_{i \rightarrow j}^{mid} \cos \lambda_i^{mid} / (\cos d_{i \rightarrow j}^{mid} - \sin \lambda_i^{mid} \sin \lambda_i^{offset}) \right] \quad (13)$$

$$\tau_i^{offset} = \text{mod}(\tau_i^{mid} - \Delta \tau_i + \pi, 2\pi) - \pi \quad (14)$$

Here $\phi_i = \theta_{i \rightarrow j}^{mid} \pm n_i \Delta \theta$ where $\theta_{i \rightarrow j}^{mid}$ is the great circle course angle between the i^{th} and j^{th} mid-point, $n_i \in [1, \dots, N^{offset}]$ is the index of the i^{th} upper/lower offset point, N^{offset} is the number of upper or lower offset points, and $\Delta \theta$ is the upper/lower angular offset. Using the positive sign in the expression for ϕ_i gives rise to the points that will be referred to as the “upper-offset” points, while the negative sign in this expression will be used when generating the “lower-offset” points. Additionally, d_{offset} is the distance from the i^{th} mid-point at which to construct the upper/lower offset point, and $d_{i \rightarrow j}^{mid}$ is the great circle distance between the i^{th} and j^{th} midpoint. It is important to note that collectively, the set of midpoints, upper-offset points, and lower-offset points comprise the complete set of states, x_k , that are discussed in Section II.A.

The last and final step of the DP grid generation process entails connecting the relevant midpoints and the upper/lower-offset points (i.e., the states, x_k). This process effectively defines the set of admissible controls, U_k , that are available at each stage. Starting with the midpoints, a segment is drawn that connects $(\lambda_i^{mid}, \tau_i^{mid})$ with $(\lambda_{i-1}^{mid}, \tau_{i-1}^{mid})$ and $2N^{offset}$ segments are drawn between $(\lambda_i^{mid}, \tau_i^{mid})$ and $(\lambda_{i-2}^{offset}, \tau_{i-2}^{offset})$. Notice that the existence of N^{offset} upper points and N^{offset} lower points are assumed. Using this process, the seven dashed, blue edges depicted in Fig. 3 are constructed. Next, segments are drawn that connect each upper/lower offset point, $(\lambda_i^{offset}, \tau_i^{offset})$, with their respective upper/lower points denoted by $(\lambda_{i+1}^{offset}, \tau_{i+1}^{offset})$. Note that the upper and lower offset points are not connected as part of this process (e.g., in Fig. 3, $(\lambda_0^{upper}, \tau_0^{upper})$ is not connected to $(\lambda_1^{lower}, \tau_1^{lower})$). Finally, the upper/lower-offset points are connected to the midpoints by constructing a segment between $(\lambda_i^{offset}, \tau_i^{offset})$ and $(\lambda_i^{mid}, \tau_i^{mid})$. This process of constructing connecting segments that originate at the upper/lower-offset points, gives rise to the three solid-red segments and three dash-dot-green segments in Fig. 3.

Once a grid has been created, the recursion relation presented in Eq. (4) is used to incrementally construct the wind-optimal route from the destination airport that is labeled “START” in Fig. 3 to the origin airport that is labeled “END.” The optimal sub-route to any node in this grid is determined by calculating the minimum total incremental cost associated with traveling from the “START” node to the node of interest. For example, to calculate the optimal sub-route from the “START” node to the node labeled $(\lambda_0^{lower}, \tau_0^{lower})$ the minimum of $C((\lambda_0^{lower}, \tau_0^{lower}) \rightarrow (\lambda_2^{mid}, \tau_2^{mid})) + C(\lambda_2^{mid}, \tau_2^{mid})$ and $C((\lambda_0^{lower}, \tau_0^{lower}) \rightarrow (\lambda_1^{lower}, \tau_1^{lower})) + C(\lambda_1^{lower}, \tau_1^{lower})$ is selected. Here $C((\lambda_0^{lower}, \tau_0^{lower}) \rightarrow (\lambda_2^{mid}, \tau_2^{mid}))$ is the cost associated with routing from $(\lambda_0^{lower}, \tau_0^{lower})$ to $(\lambda_2^{mid}, \tau_2^{mid})$ using Eq. (15), $C((\lambda_0^{lower}, \tau_0^{lower}) \rightarrow (\lambda_1^{lower}, \tau_1^{lower}))$ is the cost associated with routing from $(\lambda_0^{lower}, \tau_0^{lower})$ to $(\lambda_1^{lower}, \tau_1^{lower})$, $C(\lambda_2^{mid}, \tau_2^{mid})$ is the minimum incremental cost to arrive at $(\lambda_2^{mid}, \tau_2^{mid})$ from “START,” and $C(\lambda_1^{lower}, \tau_1^{lower})$ is the minimum incremental cost to arrive at $(\lambda_1^{lower}, \tau_1^{lower})$ from “START.”

An example of the dynamic programming grid that was used to generate the results in Section IV is illustrated in Fig. 4. This grid extends from Los Angeles, CA, $(\lambda_5^{mid}, \tau_5^{mid}) = (33.94^\circ, -118.41^\circ)$, to Honolulu, HI, $(\lambda_0^{mid}, \tau_0^{mid}) = (21.32^\circ, -157.92^\circ)$ and was created with the following grid generation parameters: $N^{offset} = 10$, $N^{mid} = 5$, $\Delta\theta = 3^\circ$, and $f_i \in \{1/5, 2/5, 3/5, 4/5\}$. With these settings, 86 nodes and 751 corresponding arcs are used to define the search space over which the wind-optimal route will be calculated. Recall that the incremental cost that is given by Eq. (15) must be calculated along each of these 751 arcs. The thin, blue lines in Fig. 4 depict the allowed segments that connect the midpoints with the upper/lower-offset points; the red lines depict the allowed segments that connect the upper-offset points together and connect the upper-offset points with the midpoints. Lastly, the green lines depict the connections between the lower-offset points and the connections between the lower-offset points and the midpoints. The thick, blue line segment depicts the corresponding wind-optimal route between Los Angeles and Honolulu that is generated using the methodology outlined in Section II.A. For reference, the contours of the magnitude of the wind velocity that were used in generating the wind-optimal route are also depicted in Fig. 4 along with the corresponding wind magnitude legend. It is important to note that the values of N^{offset} , N^{mid} , $\Delta\theta$, and f_i have been selected so as to provide a reasonable search space (i.e., approx. 250 nmi lateral deviation above and below the great circle route) for identifying a wind-optimal route, while at the same time ensuring that routes can be generated in real time. Consequently, the routes generated and analyzed in Section IV are locally, but not necessarily globally, optimal. A more thorough discussion of the results of the wind-optimal routing algorithm is reserved for Section IV.

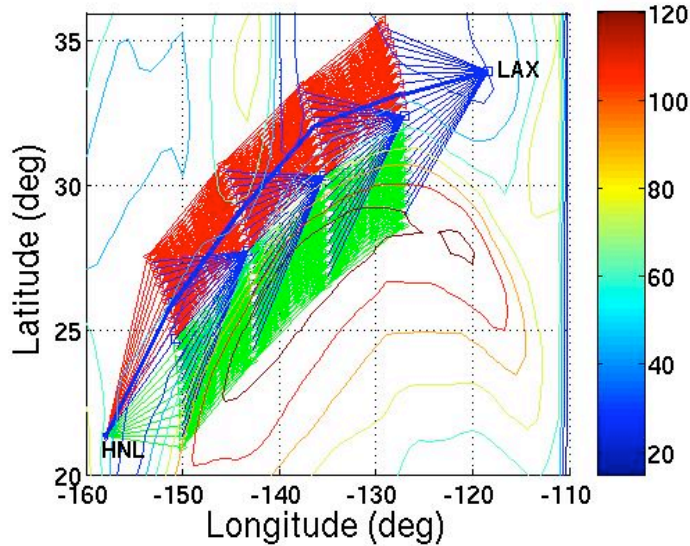


Figure 4. Dynamic programming grid and wind-optimal route between Los Angeles, CA and Honolulu, HI.

III. Unmodified Flow Characteristics

This section describes the data sources used and familiarizes the reader with the nominal characteristics of the east- and westbound traffic flying along the CEP routes. Aircraft flight plans, flight plan amendments, departure times, arrival times, and position reports were obtained from an Aircraft Situation Display to Industry (ASDI) data feed^{13,14} for December 14-16 and 19-20 of 2005. For reference, Dec. 14th is a Wednesday and Dec. 20th is a Tuesday. To filter the east- and westbound CEP route traffic from the national data mosaic provided by the ASDI data feed, only flights that explicitly contained R463, R464, R465, R576, R577, R578, and R585 in either a flight plan or flight plan amendment message were retained for further processing. The resulting aircraft counts for this five-day period are shown in Fig. 5. A total of 516 westbound and 395 eastbound flights were analyzed. The average daily west- and eastbound traffic count was 103 and 79, respectively. The exact cause of the differences between the number of arriving and departing flights is unknown and outside the scope of this paper, but is surmised to reflect the travel patterns of the largely tourist-based clientele destined for the Hawaiian Islands and a potential lack of oceanic track messages (i.e. TO messages) in the ASDI data feed. A more thorough analysis investigating the arrival and departure rates into the Honolulu ARTCC (ZHN) over several months would be required to more fully understand the east- and westbound traffic count patterns observed in Fig. 5. Additionally, merging the ASDI data feed used in this study with ATOP derived data (e.g., additional aircraft position reporting messages) would resolve any potential data drop issues.

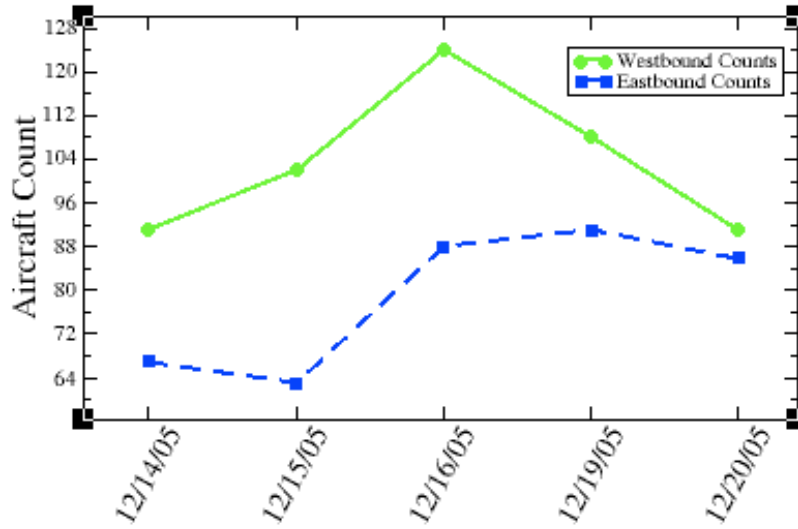


Figure 5. Total east- and westbound CEP traffic on Dec. 14-16 and Dec. 19-20, 2005.

Another useful metric for characterizing the distribution of traffic in the Central East Pacific is the vertical distribution of flights in the Oakland Oceanic airspace. To better understand this metric, the actual flight level at which the 911 east- and westbound flights entered and exited the oceanic airspace was recorded, and the results are presented in Fig. 6. The left-most image in this figure depicts the flight level at which a flight entered the oceanic airspace and the right-most figure depicts the flight level at which flights exited the oceanic airspace. For reference, flights approaching or departing the West Coast of the U.S. crossed into the oceanic airspace between 120° and 127° west longitude, while flights from Hawaii, either entered or exited the oceanic airspace between 150° and 156° west longitude. The actual locations and times of the oceanic entry/exit events were recorded while operating the Future ATM Concepts Evaluation Tool (FACET)¹⁵ in the system's playback mode. For reference, FACET is an air traffic management (ATM) modeling and simulation capability being developed by NASA. The general purpose of FACET is to provide an environment for the development and evaluation of advanced ATM concepts, such as wind-optimal routing in the Central East Pacific Ocean.

From the results presented in Fig. 6, the mean oceanic entry flight level for the eastbound flights is seen to be 351 with a standard deviation of 21, while the mean of the westbound flights is 338 with a standard deviation of 20. For flights exiting the oceanic airspace, the mean oceanic exit flight level for the eastbound flights is 362 with a standard deviation of 23, and the mean exit flight level for the westbound flights is 346 with a standard deviation of

23. Comparing the entry/exit flight levels for either the east- or westbound flights, one finds that the exit flight level is on average higher than the entry flight level. Intuitively, this is the expected outcome, since an aircraft’s “optimal” flight level increases with decreasing weight.

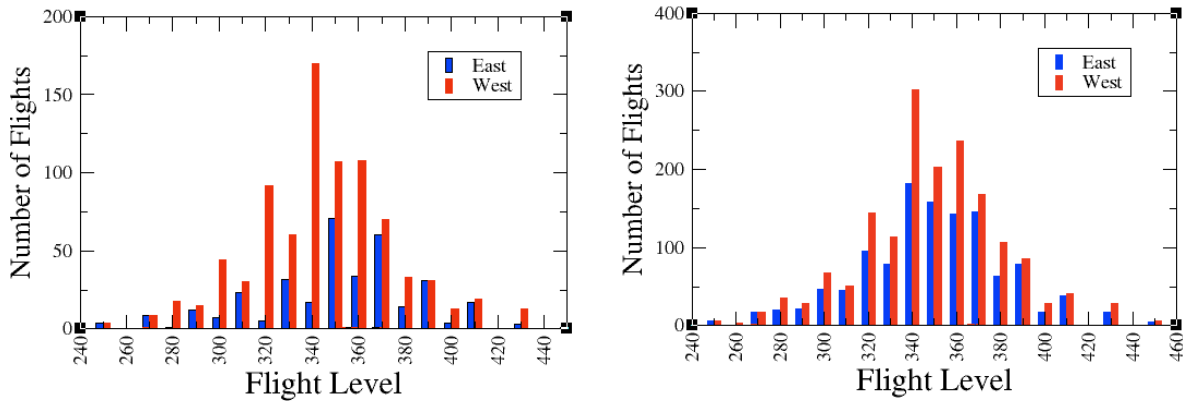


Figure 6. Vertical distribution of the east- and westbound flights upon entering (left) and exiting (right) the Oakland Oceanic Airspace.

Another key feature used to characterize the nominal flow of traffic was the temporal distribution of these flights along the fixed CEP route structure. This metric is useful for identifying arrival and departure pushes to and from the Hawaiian Islands. In Fig. 7, the oceanic entry and exit counts as a function of time are displayed for both the eastbound and westbound flights for the five days analyzed. Although minor deviations in the aircraft counts are observed when comparing the data across multiple days, several prominent features can be extracted. Starting with the eastbound oceanic entry counts (top-left), a small peak in the traffic counts is observed at 4:30 UTC followed by a larger peak at 10:00 UTC. Since flights departing HNL take approximately 45 minutes to enter the oceanic airspace, these two peaks correspond to eastbound Hawaiian flights that are departing at 5:45 pm and 11:15 pm Hawaii-Aleutian Standard Time (HST), respectively. As the eastbound Hawaiian departures exit the oceanic airspace, these flights give rise to the aircraft counts that are shown in the top-right image of Fig. 7. This figure shows a cluster of flights exiting the oceanic airspace at around 7:30 UTC and a prominent peak near 13:00 UTC. Since flights departing Hawaii spend roughly 3 to 3.5 hours in the oceanic environment en route to the west coast of the U.S., these two features correspond to the aforementioned 5:45 pm and 11:15 pm HST departures exiting the oceanic airspace.

The last two images (bottom-left and bottom-right) in Fig. 7 correspond to the oceanic entry and exit aircraft counts for the westbound flights. Beginning first with the oceanic entry counts, two broad features are observed. The first is a cluster around 2:00 UTC and the second more prominent feature that is clustered around 18:00 UTC. Since travel time from a west coast airport to the oceanic center boundary takes approximately 50 minutes (based on the flight time from LAX), these two features correspond roughly to the 5:10 pm and 11:10 am Pacific Standard Time (PST) departure pushes from the west coast. As these flights cross the Central Pacific, they reemerge at the ZHN boundary after approximately 3.5 hours of flight in oceanic airspace. The entry of these flights into ZHN airspace is evident in the bottom-right image in Fig. 7, where a cluster of flights crosses into ZHN at approximately 5:30 UTC, while a second more prominent group of flights enters ZHN airspace at approximately 21:30 UTC.

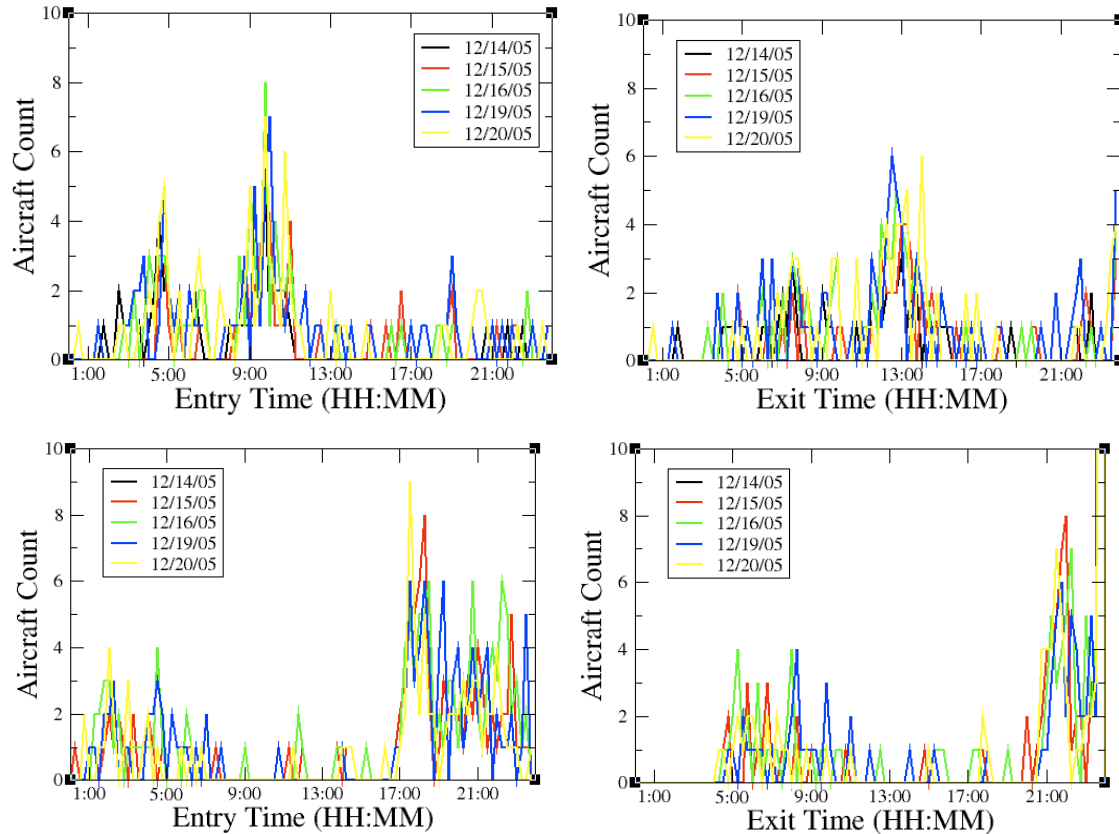


Figure 7. Eastbound oceanic entry (top-left) and exit (top-right) counts and westbound oceanic entry (bottom-left) and exit (bottom-right) counts along the CEP routes.

For the flights considered in this study, the total oceanic transit time is fairly constant and generally varies between 3 and 4 hours. The dispersion observed in the peaks in Fig. 7 therefore is more strongly influenced by the destination airport and the airline’s schedules than the total time spent traveling in the oceanic environment. To gain more insight into the origin and destination airports that are frequented by flights on the CEP routes, Fig. 8 contains departure airport usage statistics (left image) and arrival airport usage statistics (right image) for the westbound CEP flights.

For the departure statistics, only the top 21 airports are illustrated, although flights were observed to depart from 41 airports during the five-day period analyzed. Roughly 44% of all westbound flights departed from Los Angeles International Airport, KLAX, and San Francisco International Airport, KSFO. The names associated with the remaining departure airport acronyms in Fig. 8 follow: Chicago O’Hare (KORD), McCarran Intl. (KLAS), Ontario Intl. (KONT), Phoenix Sky Harbor Intl. (KPHX), John Wayne Airport (KSNA), Oakland Metropolitan Intl. (KOAK), Dallas/Fort Worth Intl. (KDFW), San Diego Intl. (KSAN), Portland Intl. (KPDX), Memphis Intl. (KMEM), Vancouver Intl. (CYVR), Norman Y. Mineta San Jose Intl. (KSJC), Seattle-Tacoma Intl. (KSEA), Sacramento Intl. (KSMF), Salt Lake City Intl. (KSLC), Houston Intl. (KIAH), Atlanta Intl. (KATL), Van Nuys (KVNY), and Minneapolis-St. Paul Intl. (KMSP).

The arrival airport statistics in the rightmost image of Fig. 8, illustrate that approximately 63% of all flights destined for Hawaii landed at Honolulu Intl. Airport (PHNL). In contrast, only one flight landed at Lanai (PHNY) and two flights landed at Hilo (PHTO) during the same five-day period. Of the remaining flights, 22% landed at Kahului (PHOG), 9% landed at Kona/Keahole Kailua (PHKO), and 5% landed at Lihue/Kauai Island (PHLI).

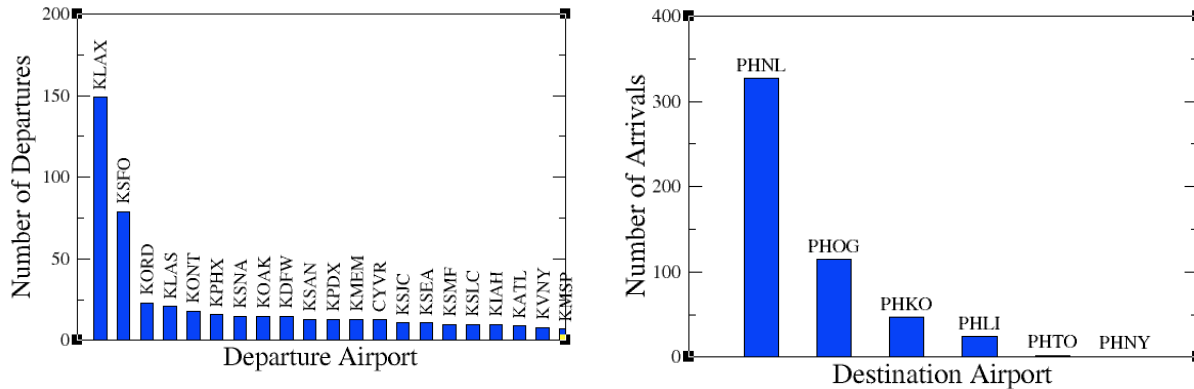


Figure 8. Most frequented departure (left) and destination (right) airports for the westbound CEP flights on Dec. 14-16 and 19-20, 2005.

The last metric used to examine the characteristics of the traffic arriving at and departing from Hawaii is the distribution of these flights among the CEP routes. This metric is believed to be the most sensitive to seasonal variations in the wind fields, but the distribution observed in Fig. 9 should be typical of the distribution that is commonly observed during the winter months. As shown in Fig. 9, the westbound flights traveled predominately along R464 and R576, while the eastbound traffic predominately flew along R465 and R577. All four of these routes are unidirectional. Significantly less traffic was observed along R463 and R578, which are bi-directional routes. The control of flights along these routes was distributed roughly evenly between OC-3 and OC-4. As illustrated by Fig. 2, traffic on R576, R577, and R578 is controlled by OC-3, while traffic on R463, R464, R465 and R585 is controlled by OC-4.

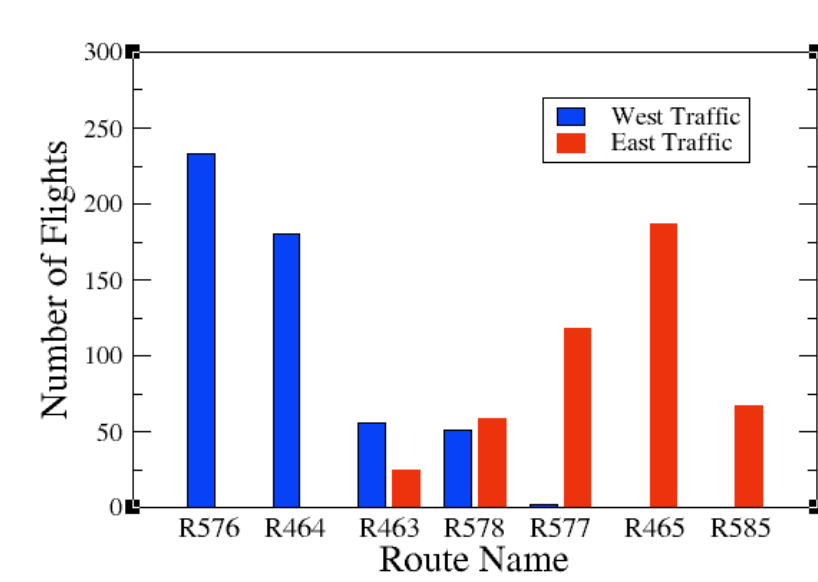


Figure 9. East- and westbound CEP route usage statistics.

IV. Wind Optimal Routing Analysis

The results from a set of simulations to assess the potential benefits and consequences of allowing flights to deviate from the fixed, nominal (CEP route) structure in favor of user-preferred routes are presented in this section.

Using the ASDI data files and the wind fields from the Global Forecast System (GFS) Atmospheric Model¹⁶ for Dec. 14-16 and 19-20 of 2005, three sets of simulations were run in FACET. In the first set of simulations, flights traveled along their filed flight plans, as specified in the ASDI files. For the second set of simulations wind-optimal trajectories were generated roughly within the oceanic center boundary (OCB), while in the third set of simulations a wind-optimal trajectory was generated from the flight’s origin to the destination (OD).

The first set of simulations was designed to serve as a surrogate for current day routing options. FACET could have been operated in a playback mode in which the actual aircraft position reports from ASDI would have been processed, as was done in Section III, but later comparisons between the playback results and the wind-optimal results would have included not only the routing differences but also any aircraft performance modeling differences as well. To generate the results for the second set of simulations (i.e. the OCB wind-optimal results), route generation began at the first waypoint prior to entering one of the CEP routes and ended after the first waypoint immediately following the last CEP route appearing in the nominal flight plan.

The remainder of this section is structured as follows. In subsection IV.A, the modified traffic pattern characteristics are examined for the three simulations. To assess the potential impact that the wind-optimal routes might have on the air traffic service provider, the sector count differences and first-loss-of-separation statistics are presented in subsection IV.B and IV.C, respectively. These metrics are being presented because significant increases in either of these values may substantially increase controller workload. Finally, the time- and distance-savings statistics for both wind-optimal routing simulations are presented in subsection IV.D.

A. Traffic Patterns

In this section, the individual and aggregate traffic pattern characteristics are examined for flights on both the nominal CEP-based routes and the two wind-optimal routes. As an example of these different routing scenarios, consider the three routes between ORD and HNL in Fig. 10. The solid green route that is labeled “CEP” in this figure is the nominal flight plan that was filed by a major U.S. air carrier on Dec. 14, 2005 between this city pair. The solid magenta line labeled “OCB” is the corresponding OCB wind-optimal route for this flight. In calculating this route, route generation began at the “BEBOP” fix, which lies near the ZOA-OAO boundary, and continued up to the “BITTA” fix, which lies near the OAO-ZHN boundary. Finally, the red line in this figure that is labeled “OD” depicts the wind-optimal route that was generated between ORD and HNL. As expected, the amount of variance between the “CEP” and “OD” routes is significantly larger than the variance between the “OCB” and “CEP” routes.

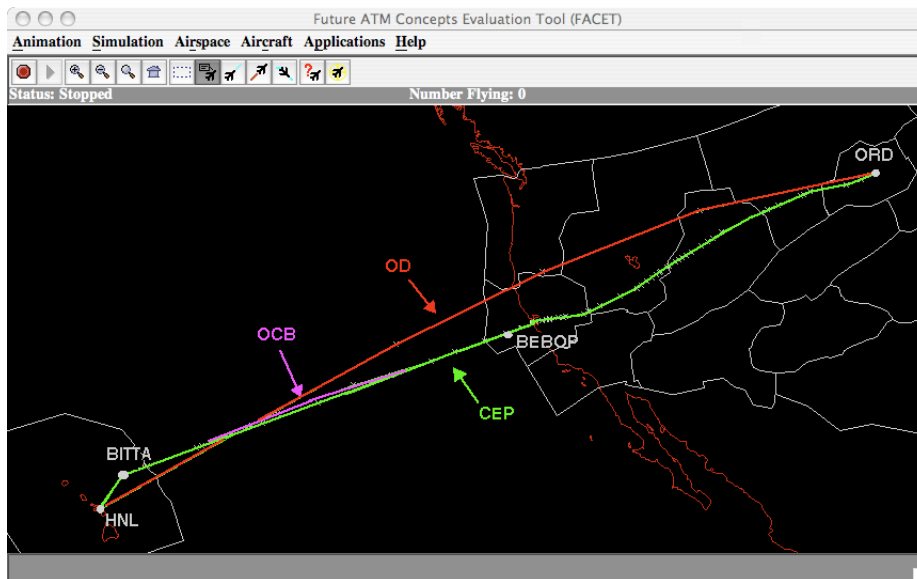


Figure 10. Fixed versus wind-optimal routes between ORD and HNL.

Since the magnitude and direction of the winds that were used have such a significant impact on the results, a brief discussion regarding the coverage and characteristics of the National Oceanic and Atmospheric Administration

(NOAA) atmospheric model is appropriate. GFS is a global atmospheric model with a horizontal resolution of approximately $0.5^\circ \times 0.5^\circ$ latitude/longitude and an unequally spaced vertical resolution starting at 1000 mb (surface) and extending up to 100 mb. Updates to the GFS model are available every six hours and forecasts are available up to 16 days into the future. As an example of the wind fields that were used, the 00:00 UTC, zero hour forecast wind magnitude contours at 250 mb., which roughly encompasses flight levels 310 through 360 over the Central East Pacific, are shown in Fig. 11. The top-left image in this figure contains the contours for Dec. 14th, the top-right image shows the Dec. 15th data, the middle-left image shows the Dec. 16th data, the middle-right image shows the Dec. 19th data, and finally the bottom image shows the contours for Dec. 20th. The legend associated with the wind magnitude contours follows: > 120 kts., magenta; >105 kts., red; >90 kts. orange; >75 kts., yellow; >60 kts., light green; >45 kts., dark green; >30 kts, light blue; >15 kts, blue; and >0 kts, dark blue. Although the direction of the wind field is not illustrated in these images, the winds are generally westerly (i.e., flowing west to east) in this region of the Pacific Ocean. For reference, the Hawaiian Islands are shown at the bottom left of each image in Fig. 11 and the west coast of the United States is shown on the right side of each image. A region of very strong, westerly winds (>120 kts.) is shown in each of these figures and the location of these strong winds tended to move in a northerly direction during the five day period that was examined in this study. As expected, the variable wind fields illustrated in Fig. 11 had a significant impact on the wind-optimal routes and will now be explored in more detail.

The band of strong winds (>100 kts) that is exhibited in Fig. 11 is most likely the polar jet stream¹⁷ that is often located in this region during the winter. The westerly winds within the core of this jet stream often exceed 100 kts., as illustrated, and can reach speeds as high as 250 kts. During the summer months, this jet stream tends to weaken and move farther north towards Canada. Since the results of the wind-optimal routing algorithm are, by nature, susceptible to the magnitude and direction of the wind field in which the routing is being performed, the results in this study should represent an upper bound on the maximum savings and impact that can be expected in this region of the ocean. A follow-on study that examines the seasonal savings and impact of wind-optimal routing in the Pacific Ocean would be beneficial.

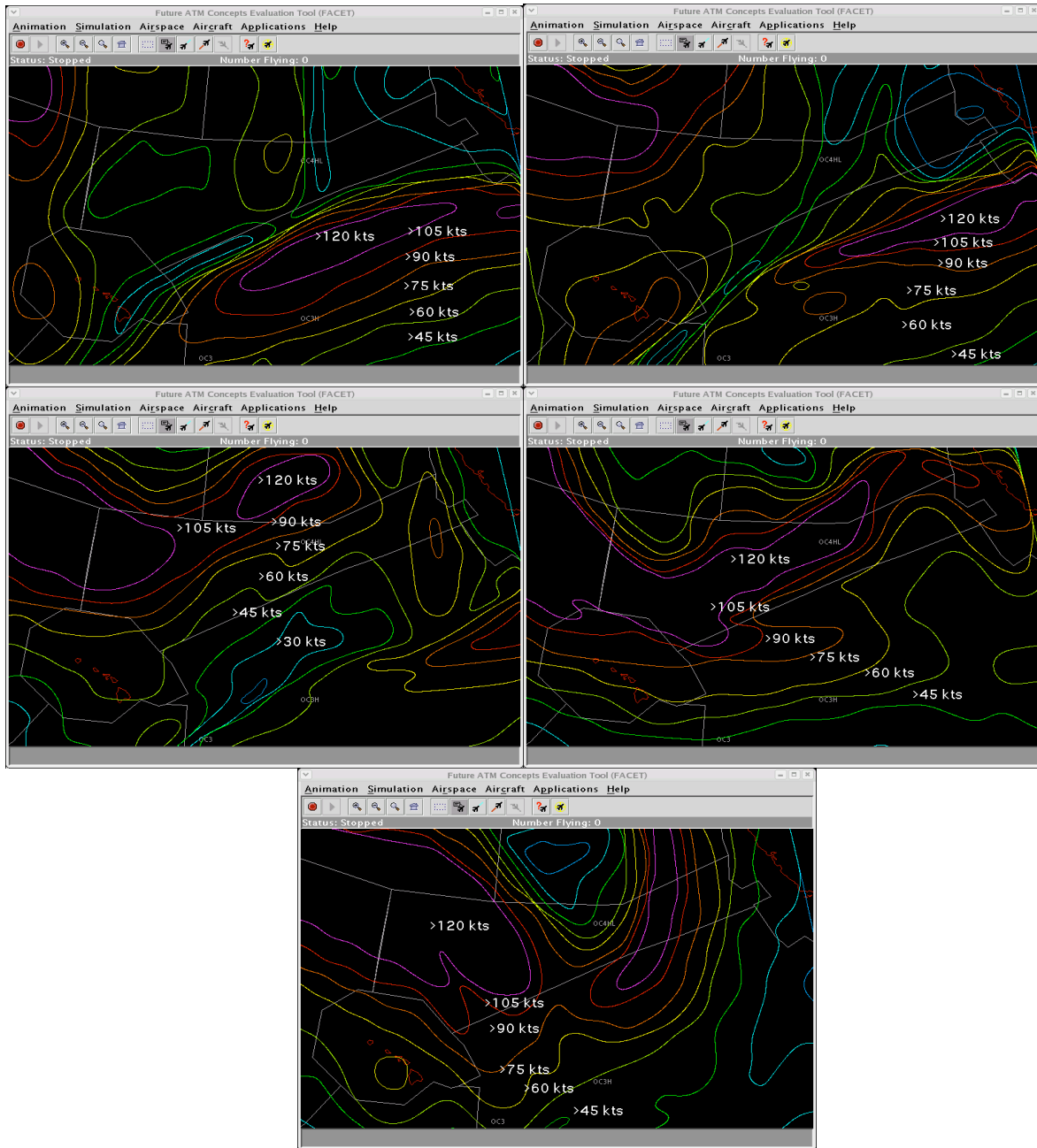


Figure 11. GFS wind contours at 250 mb for Dec. 14th (top-left), Dec. 15th (top-right), Dec. 16th (middle-left), Dec. 19th (middle-right), and Dec. 20th (bottom) in the Central East Pacific.

To illustrate the impact that the varying wind fields can have on an individual flight, consider the flight plans depicted in Fig. 12. The nominal, westbound flight plan, which is represented by the orange line labeled “CEP,” was filed and flown by a major U.S. carrier on Dec. 14, 2005. The total path distance of this route is 2,305 nmi and the total travel time is 4.52 hrs. The corresponding westbound wind-optimal routes that were generated directly from LAX to HNL using the wind fields illustrated in Fig. 11 are also shown in this image and drawn as follows: red line, Dec. 14th winds; yellow line, Dec. 15th winds; green line, Dec. 16th winds; blue line, Dec. 19th winds; and purple line, Dec. 20th winds. The maximum lateral spread between the westbound wind-optimal routes is 130 nmi and the maximum lateral offset from the westbound CEP-based flight plan route in the oceanic center varies from 120 to 260 nmi. The total path distance of these wind-optimal routes varies between 2218 and 2226 nmi, and the total

travel times vary between 4.3 and 4.5 hrs. For this case, it is interesting to note that the CEP-based flight plan travels exclusively through OC-4, whereas four of the wind-optimal routes travel through both OC-3 and OC-4 and one of the wind-optimal routes (generated using the winds for Dec. 16th) traveled exclusively through OC-4.

As expected, the dispersion observed for the westbound wind-optimal routes is also observed for the eastbound flights. To illustrate this point, the right-most image in Fig. 12 depicts both a nominal CEP-based flight plan as well as the five wind-optimal routes that were generated using the aforementioned wind fields. The CEP-based flight plan that is depicted by the orange line labeled “CEP” was filed and flown by a major U.S. carrier on Dec. 14th from HNL to LAX. The total path distance of this route is 2278.5 nmi, and the total travel time was 5.12 hrs. The legend associated with the five wind-optimal routes follows: red line, Dec. 14th winds; yellow line, Dec. 15th winds; green line, Dec. 16th winds; blue line, Dec. 19th winds; and purple line, Dec. 20th winds. The total path distances of these wind-optimal routes vary between 2215.8 and 2220.7 nmi, and the total travel times vary between 5.0 and 5.1 hrs. As seen from this figure, the wind-optimal route generated with the wind field from Dec. 14th (red line) most closely matches the filed CEP-based flight plan. Of the five wind-optimal routes, four of the routes travel almost exclusively through OC-3, while the route generated using the wind field for Dec. 16th passed almost entirely through OC-4. The maximum lateral deviation between the eastbound wind-optimal routes is approximately 190 nmi and the lateral offset from the CEP-based route varies from 60 to 230 nmi within the Oakland Oceanic airspace.

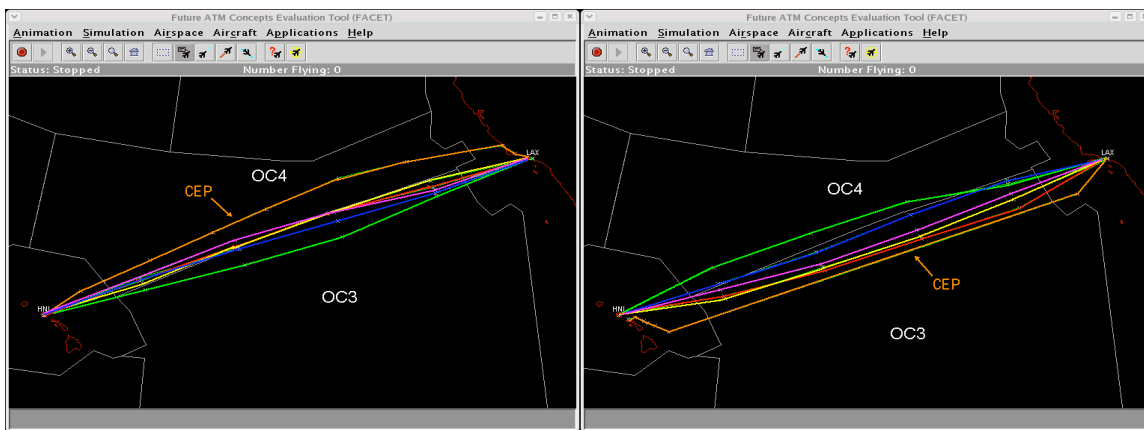


Figure 12. Wind-optimal westbound (left) and eastbound (right) flight plans using Dec. 14-15th and 19-20th, 2005 wind fields.

The previous example explored the simple case in which a time varying wind field impacted an individual flight. A far more challenging and interesting problem is to explore the impact of this wind field on a larger collection of flights under the three simulation scenarios that were previously described. To conclude this subsection, FACET images depicting aircraft position (latitude and longitude) histories for west- and eastbound CEP-flights will be examined to gain a qualitative understanding of the impact that the wind field and simulation modes have on groups of flights. Later in subsection IV.B through IV.D these differences will be quantified by examining sector counts, conflict counts, and path length differences.

Figure 13 contains a total of six images representing the east- and westbound aircraft position histories that were generated by using the ASDI and the 0:00 UTC, zero-hour forecast GFS wind field data from Dec. 14. The three images in the left most column show histories for eastbound flights (cyan lines), while the three images in the right most column show the histories for the westbound flights (green lines). The first row of images was generated by running FACET in the simulation mode in which the filed flight plan was flown; the second row contains results from the wind-optimal OD mode; and the last row contains results from the wind-optimal OCB mode. The most important features to note in these images pertain to the amount of structure and the distribution of the flights under the three routing scenarios. The CEP-based flight plan simulation results (top row) and the wind-optimal OCB results (bottom row) maintain a high-level of structure to the traffic pattern, while the wind-optimal OD routes (middle row) contain virtually no structure. On first glance, the wind-optimal OCB routing also tends to maintain the original OC-3 and OC-4 sector loading distribution, whereas the wind-optimal OD routing algorithm appears to significantly alter this distribution. A qualitative discussion of the differences between these data sets will ensue in the forthcoming subsections.

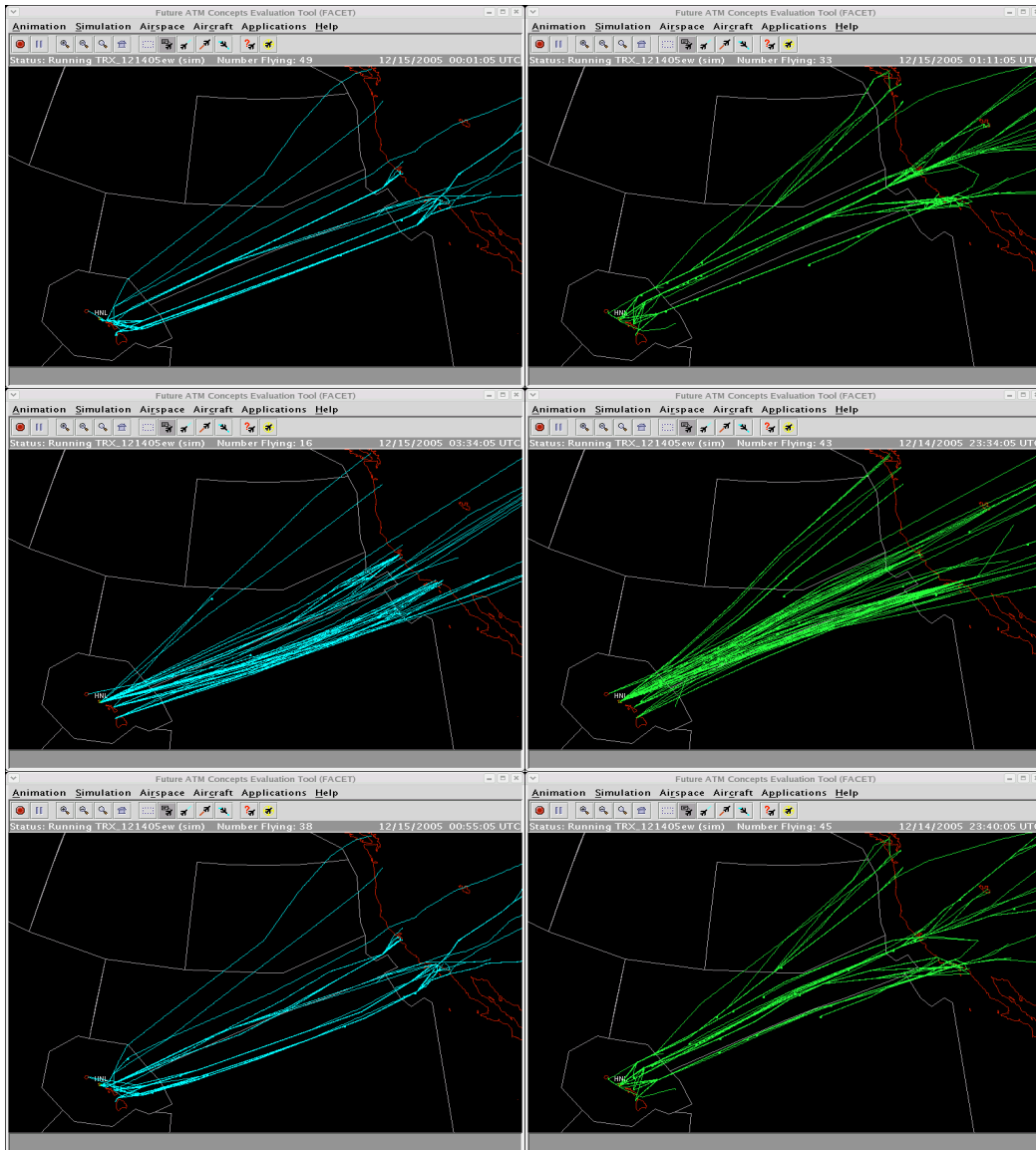


Figure 13. Flight Histories for Dec. 14, 2006 for eastbound, nominal (CEP) routes (top-left), westbound nominal (CEP) routes (top-right), eastbound OD routes (mid-left), westbound OD routes (mid-right), eastbound OCB routes (bottom-left), and westbound OCB routes (bottom-right).

B. Sector Counts

To quantify the impact that wind-optimal routing can have on the airspace, this section contains both detailed sector count differences for Dec. 14th and aggregate sector count differences for the five-day period. Beginning first with the detailed sector count differences shown in Fig. 14, several features are worth noting. The left-most image in this figure contains the OC-3 sector counts as a function of time, and the right-most image contains the OC-4 sector counts. In each image, three different curves are presented that represent the number of unique flights observed in a 15-minute period as a function of time. The black curve labeled “FP Simulation” contains the counts resulting from operating FACET in the simulation mode in which aircraft followed their CEP-based flight plan routes, the red line corresponds to the counts when FACET is operated in the wind-optimal OD mode, and finally the blue line corresponds to the results from a FACET wind-optimal OCB simulation. As expected, both the CEP-based flight plan simulation results and the wind-optimal OCB results are in good agreement, and only minor

differences between these results are observed. The wind-optimal OD simulation results, on the other hand, exhibit slightly more differences, and several instances in which significant numbers of flights operated in different sectors can be observed. For example, between 1:00 and 4:00 UTC there was notable increase in the OC-3 sector counts for the wind-optimal OD simulations and a corresponding decrease in counts in OC-4. Similar sector count differences are also apparent from 4:00 to 8:00 UTC and 13:00 to 17:00 UTC. The most significant sector count increase occurred at approximately 4:00 UTC in OC-4. At this time, the wind-optimal OD sector count differences increase by over 30%. Although the peak count at this time was still far below the peak observed at 20:30 UTC, resource scheduling algorithms¹⁸ or dynamic re-sectorization¹⁹ could be used to reduce these counts back to nominal levels. Results for the other four days analyzed in this study show similar trends.

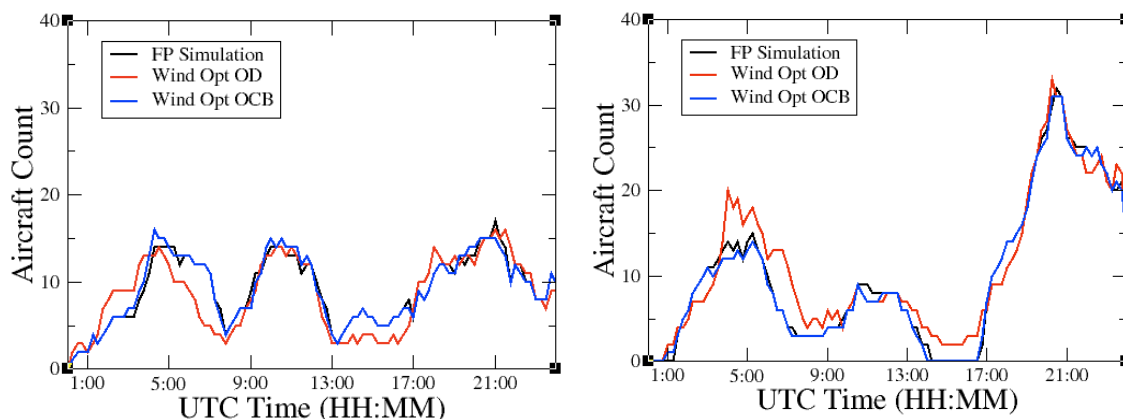


Figure 14. Oakland Oceanic Sector 3 (left) and 4 (right) sector counts for Dec. 14, 2005.

To better understand the sector count difference trends, Fig. 15 contains histograms of the sector count differences as a function of time over a five-day period for OC-3 (left image) and OC-4 (right image). The blue bars labeled “OD Routing” correspond to differences between the CEP-based flight plan simulation and the wind-optimal OD simulation results, while the red bars labeled “OCB Routing” correspond to differences between the CEP-based flight plan simulation and the wind-optimal OCB simulation results. Examining the OC-3 results first, the average sector count deviation for the “OD Routing” and “OCB Routing” results are 1.8 and -0.02 , respectively. The maximum deviations for the “OD Routing” results is 16, while the minimum deviation is -6 . Similarly, the maximum deviation observed for the “OCB Routing” case is 7, and the minimum deviation is -8 . Continuing next with the OC-4 results, the average sector count deviations for the “OD Routing” and “OCB Routing” results are -2.3 and -0.14 , respectively. The maximum deviation for the “OD Routing” results is 6, while the minimum deviation is -17 . Similarly, the maximum deviation observed for the “OCB Routing” case is 7, and the minimum deviation is -8 .

As seen from these results, the sector count difference deviations in general are minor for both the wind-optimal OD and OCB routes, however during select instances of time sizeable differences can be observed. When interpreting the minimum and maximum results, it is also important to take into consideration the frequency or number of occurrences of these large sector count deviations. For example, when the OC-4 sector count differences are examined, one finds that only 27 out of 485 time instances (or 5.6% of the instances) contained sector count deviations greater than or equal to 10 aircraft for the “OD Routing.” To address potential controller workload issues associated with these instances in which the sector count differences exceed a pre-defined threshold, the aforementioned scheduling or re-sectorization techniques may be useful for regulating the sector traffic counts.

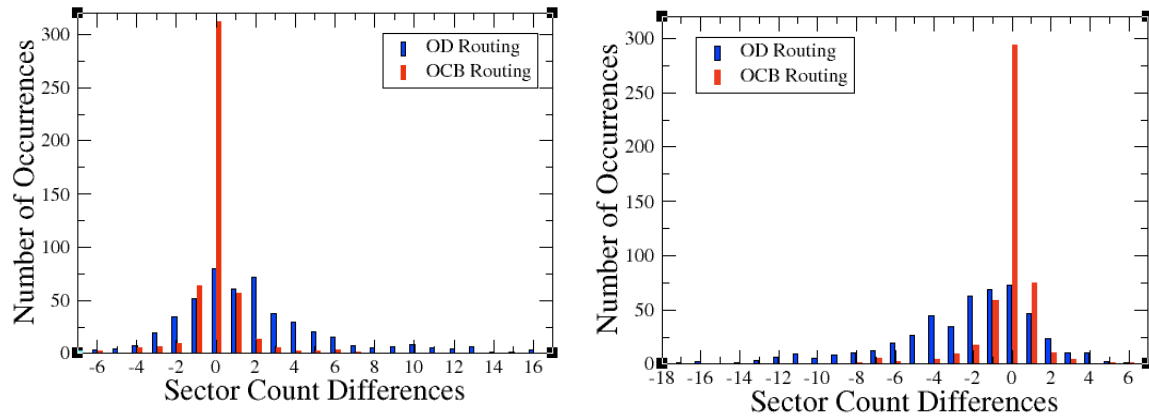


Figure 15. Aggregate Oakland Oceanic Sector 3 (left) and 4 (right) sector count differences.

C. First-Loss-of-Separation Statistics

Changes in the traffic patterns in the Central East Pacific cannot only increase the workload of a controller but can also give rise to an increase in the number of possible losses of separation. With the deployment of the new ATOP system, the FAA is proposing to reduce the separation standards on the CEP routes to 30 nmi lateral spacing, 30 nmi longitudinal spacing, and 1000 ft vertical separation. Using FACET, the simulated trajectories for all east- and westbound flights were examined for possible losses of separation on both the nominal CEP-based flight plan routes, the OD wind-optimal routes, and the OCB wind-optimal routes using these reduced separation standards and two additional sets of more restrictive standards. As previously mentioned, the separation standards for flights on the CEP routes are as follows:²

- 1,000 feet vertical separation
- 50 nmi lateral separation
- 5-10 min longitudinal separation using the “Mach Number Technique” that depends on differences in the Mach number between aircraft pairs

Since the primary focus of this study was on developing and assessing the impact of wind-optimal routes, and not on developing a conflict probe for Oakland Oceanic airspace, a decision was made to greatly simplify the definition of a first-loss-of-separation (FLOS) event in this study. Therefore, losses of separation were identified under the following three different separation criteria: (1) 30 nmi lateral spacing, 30 nmi longitudinal spacing, and 1000 ft vertical spacing; (2) 40 nmi lateral spacing, 40 nmi longitudinal spacing, and 1000 ft vertical spacing; and (3) 50 nmi lateral spacing, 50 nmi longitudinal spacing, and 1000 ft vertical spacing. For the remainder of this section, the first of these three separation standards will be referred to as the “30/30” separation standard, the second will be referred to as the “40/40” separation standards, and the last of these three will be referred to as the “50/50” separation standard. Both the lateral and longitudinal separation standards for the 30/30 cases are less restrictive than current standards. For the 40/40 cases, the lateral separation standards are less than current standards, as are the longitudinal separation standards, except when the Mach number of the leading aircraft is greater than approximately Mach 0.05 faster than the trailing aircraft. Finally, for the 50/50 cases, the lateral separation standards are the same as current day standards, and the longitudinal standards are less restrictive when the Mach number of the leading aircraft is greater than approximately Mach 0.04 faster than the trailing aircraft.²

For the remainder of this section, FLOS statistics will be presented for both a single day and aggregated over a five-day period. The geographical location for each unique, simulated FLOS event that occurred using the Dec. 16th data set is presented in Fig. 16 using both the 30/30 (left image) and the 50/50 (right image) separation standards. The red circles in both images depict the unique FLOS locations generated with the CEP-based flight plan simulations, the green squares depict the location generated with the OD wind-optimal routing, and lastly the blue triangles depict the locations resulting from the OCB wind-optimal routing simulation. For the 30/30 cases, there were 13 FLOS events for the CEP-based flight plan simulation results, 24 FLOS events for the OD wind-optimal routing simulation, and 19 FLOS events for the OCB wind-optimal routing simulation. Similarly, for the 50/50 cases, 17 FLOS events were observed for the CEP-based flight plan simulation, 48 FLOS events were observed for the OD wind-optimal routing case, and 31 FLOS events were generated for the OCB wind-optimal routing case.

It is also important to note that the FLOS events depicted in Fig. 16 take place at a wide range of flight levels. For example for the 17 FLOS events associated with the CEP-based flight plan simulations, events were observed at six different flight levels ranging from 320 through 370. With regard to the geographical location of the FLOS events depicted in this figure, there were numerous events near the oceanic center boundary, which presumably would never have occurred if the planes had passed from the Center airspace (e.g. ZHN and ZOA) into the oceanic airspace properly spaced. Recall that the separation standard in the Center airspace is only five nmi in the lateral and longitudinal domain and 1,000 ft in the vertical domain. This refinement would be beneficial to study in more detail as part of a future study. Another feature to note is the large number of FLOS events, especially for the OD wind-optimal simulation case, that occur at the boundary between OC-3 and OC-4. A large number of these events are associated with the westbound traffic streams that were observed to converge on this day at the boundary (see the middle images in Fig. 13 for example).

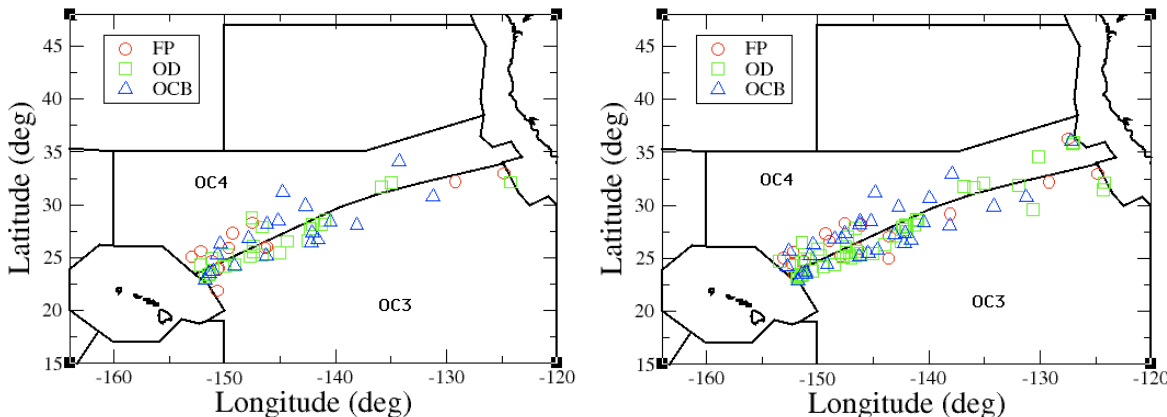


Figure 16. Simulated first-loss-of-separation locations using 30/30 (left) and 50/50 (right) latitudinal/longitudinal separation standards for Dec. 16, 2005

To begin understanding the potential long-term implications of reducing the separation standards in the Central East Pacific, aggregate FLOS statistics are presented in Fig. 17. The left-most image in this figure contains the aggregate, five-day FLOS counts for the three different FACET simulations, assuming the following separation standards: 30/30, 40/40, and 50/50. As expected, the number of FLOS events tends to increase with increasing separation standards, and the rate of increase amongst the three different simulations is roughly equal. For all separation standards, the OD wind-optimal routing results lead to the largest number of FLOS events, while the CEP-based simulation results lead to the least number of events. This is to be expected, since the OD wind-optimal routes tend to allow streams of aircraft departing from different areas to converge, whereas the CEP-based routes tend to isolate the predominant traffic streams traveling to and from Hawaii.

The second image in Fig. 17 contains the daily FLOS counts at each date for the three different FACET simulations when the 30/30 separation standards are in place. Typically, the number of FLOS events associated with the CEP-based routing is lower than the other simulation results, and the OD wind-optimal simulation results tend to yield the most number of FLOS events. The total number of FLOS events also tends to track the total aircraft counts that are displayed in Fig. 5. For example, the lowest aircraft and FLOS counts occurred on Dec. 14th, while the highest aircraft and FLOS counts occurred on Dec. 16th. Based on the results presented in this study, the number of FLOS events would significantly increase when transitioning from the nominal (CEP-based) routes to either the wind-optimal OD or OCB routes, which in turn could increase the workload of a controller handling these flights. A follow-on study that explores the use of additional control mechanisms, such as departure or speed controls, is required to determine if the number of FLOS events for the wind-optimal routes can be reduced to the CEP-routing levels.

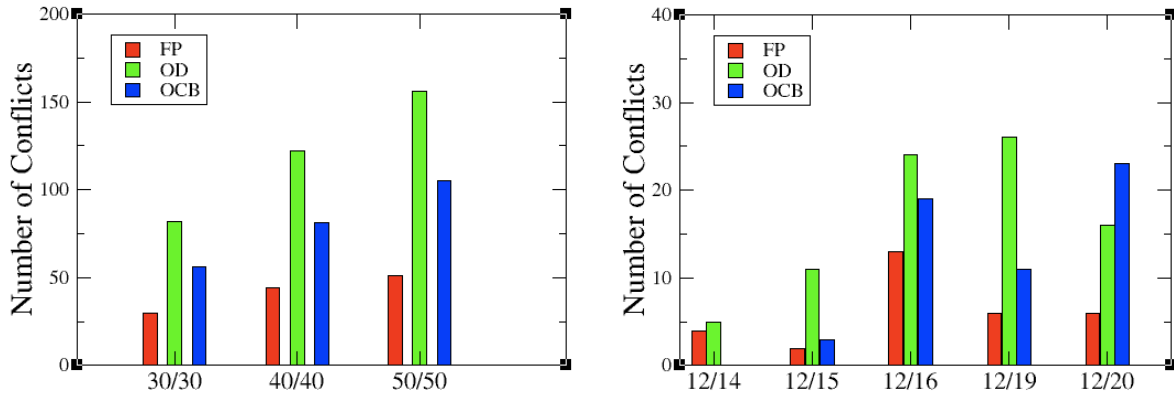


Figure 17. Aggregate simulated first-loss-of-separation events with 30/30, 40/40, and 50/50 separation standards (left) and daily events assuming 30/30 separation standards (right).

D. Path Differences

The final metrics used to quantify the impact of wind-optimal routing in the Central East Pacific are time and distance savings. Here, time savings is defined as the simulated travel time on the CEP-based routes minus the travel time on the wind-optimal routes. Similarly, distance savings is defined as the simulated travel distance on the CEP-based routes minus the travel distance on the wind-optimal routes.

This section presents both individual and aggregate savings statistics for the five-day period examined. In Figs. 18-19, the individual distance and time savings statistics for the following eight origin-destination city pairs are presented: SFO-HNL, LAX-HNL, DFW-HNL, ORD-HNL, HNL-SFO, HNL-LAX, HNL-DFW, and HNL-ORD. The SFO and LAX routes were selected because they represent the largest group of flights utilizing the CEP routes (see Fig. 8). In contrast the DFW and ORD routes, which account for a relatively minor portion of the CEP route traffic, were selected to represent the potential savings to inland origin-destination city pairs. In both figures, the left-most images contain the results from the FACET wind-optimal OD routing simulations and the right-most images contain the results from the OCB wind-optimal routing simulations. The black circles in each image depict actual savings for an individual flight on one of the analyzed days, and the red squares represent the mean savings along each route with the accompanying standard deviation.

Comparing the two images in Fig. 18, a number of noteworthy features can be observed. The most obvious and expected feature is that the time savings statistics for the OD routes tend to be slightly larger than the savings on the OCB routes. In general, the savings statistics for the central U.S. origin/destination airports tend to be slightly higher than the savings observed for the west coast origin/destination airports. The amount of dispersion in the OD data points in Fig. 18 is also seen to reduce noticeably when compared to the OCB results. For example, the time savings for the HNL-LAX route varies between zero and 38 minutes on the OD routes, but varies between zero and 20 minutes on the OCB route.

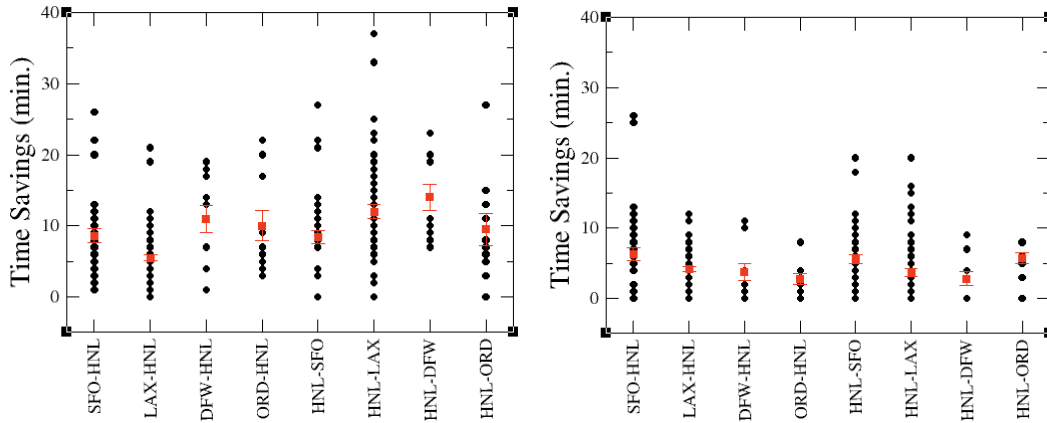


Figure 18. Wind-optimal OD (left) and OCB (right) time savings statistics for select origin-destination airport pairs

Continuing with the individual distance savings statistics that are presented in Fig. 19, a number of trends that tend to mirror the results in Fig. 18 are observed. The most notable difference between the between the OD (left image) and OCB (right image) wind-optimal routing results is the extent to which the data dispersion is reduced in the OCB simulations. For example, the distance savings results varied between 196 nmi and -16 nmi for flights traveling between SFO and HNL under the OD simulations, but the variance was only between 51 nmi and -17 nmi for the OCB results. It is worth noting that the large distance deviations (>170 nmi) that were observed for the SFO to HNL flights all occurred when using the data sets for Dec. 19th. As can be seen from the wind fields that are depicted in Fig. 11, a very strong (>120 kt) head wind existed in much of sector OC-4 on this day. In all four cases in which distance savings greater than 170 nmi were recorded, the filed flight plan routed the plane on a southerly route through OC-3, whereas the OCB wind-optimal route flew the plane on a more direct route through OC-4. Finally, a general trend can also be observed for the OD simulations in which the distance savings is greater for inland origin/destination airports (e.g. DFW and ORD) than it is for origin/destination airports on the west coast (e.g. SFO and LAX). As expected, this trend does not hold true for the OCB simulations, since wind-optimal routing is not initiated until the flight reaches the oceanic center boundary.

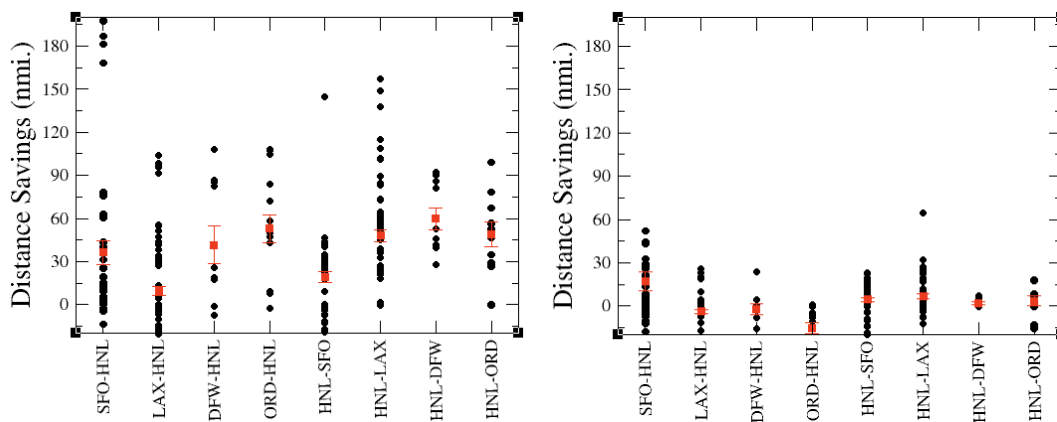


Figure 19. Wind-optimal OD (left) and OCB (right) distance savings statistics for select origin-destination airport pairs

Aggregate time and distance saving statistics for all origin-destination pairs over the five-day period examined are presented in Figs. 20 and 21. The left most image in each of these figures depicts the differences between the flight plan and OD wind-optimal routing simulations, while the right most image depicts differences between the flight plan and OCB wind-optimal routing simulations. Thirty-one time bins ranging from zero minutes of savings

to 30 minutes of savings in increments of one minute were used to classify the data appearing in Fig. 20. The average time savings for the OD simulations was 9.9 min with a standard deviation of 7.3 min, while the average time savings for the OCB simulations was 4.8 min with a standard deviation of 5.0 min. For reference, the average travel time on the nominal (CEP-based) routes over the five-days was 5.5 hrs.

A number of interesting trends are evident in the two images appearing in Fig. 20. Firstly, the time savings statistics are strongly attenuated for the OCB simulations, while the OD simulation results exhibit a large tail. In regards to the significant number of flights with time savings of 30 minutes, over half of these flights occurred with the Dec. 19th data set and could be attributed to significant differences between the filed flight plan route and the calculated wind-optimal routes. For example, in most instances flights filed through OC-4 encountered a significant head wind, while a more southerly wind-optimal route was available. These very large time savings are by no means the norm and can only be expected when (1) the polar jet stream traverses OC-3 or OC-4 and (2) the air carrier does not compensate for the prevailing wind patterns. Interestingly enough, a sizeable number of the flights with very large time savings were general aviation (GA) flights, which may not have as sophisticated routing software as the major air carriers servicing this market.

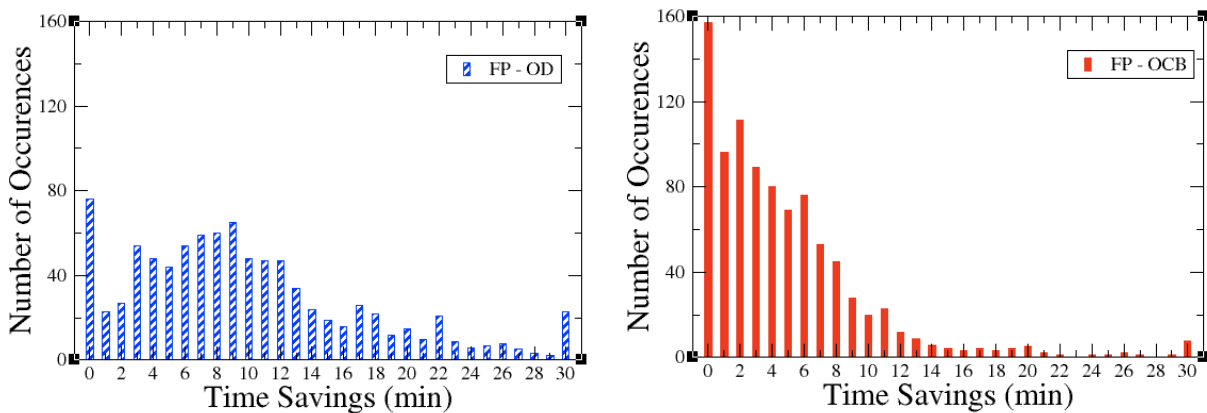


Figure 20. Aggregate wind-optimal time saving statistics for OD routing (left) and OCB routing (right)

The aggregate, five-day distance savings statistics for both the OD (left-image) and the OCB (right-image) wind-optimal routing simulations are presented in Fig. 21. Twenty-four distance bins ranging from -30 nmi to 200 nmi in steps of 10 nmi were used in creating the histograms in these figures. The average distance savings for the OD simulations was 36 nmi with a standard deviation of 42 nmi, while the average savings for the OCB simulations was 4 nmi with a standard deviation of 29 nmi. For reference, the average travel distance on the nominal (CEP-based) routes over the five-days was 2,401 nmi. The most striking difference between these two figures is the variability of the distance savings results. As previously mentioned, this is to be expected given the fact that the OD wind-optimal routing simulations provide each flight with significantly more routing variability than is provided to flights under the OCB wind-optimal routing simulations. The flights with very large distance savings (>150 nmi) are the same flights that were previously discussed in which large variations in the filed and wind-optimal routes were observed.

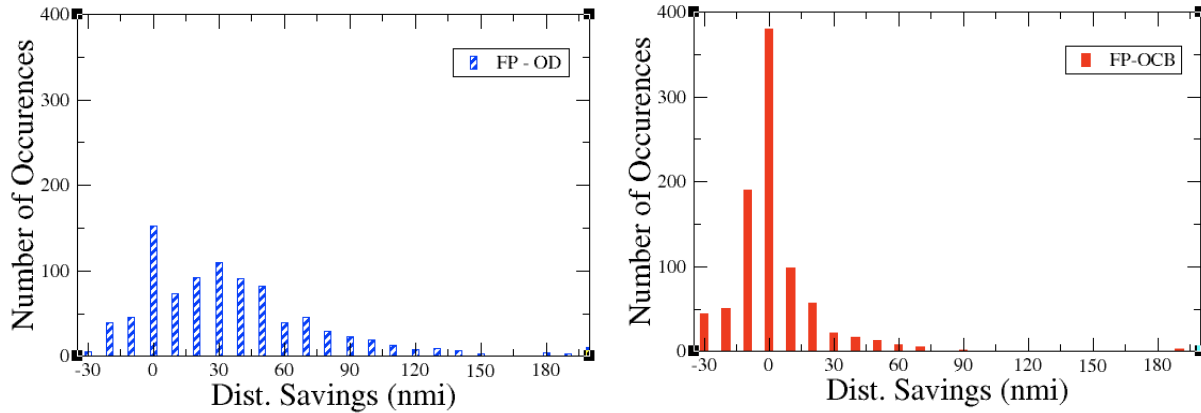


Figure 21. Aggregate wind-optimal distance saving statistics for OD routing (left) and OCB routing (right)

V. Concluding Remarks

This paper contains the results of the first extensive study designed to characterize the flow of traffic on the CEP routes and to assess the potential benefits of transitioning from these fixed routes to user-preferred routes. As a surrogate for the actual user-preferred routes, a minimum-time, wind-optimal dynamic programming algorithm was developed and utilized in this study. The results of this study are important because with the introduction of the FAA's new ATOP system at Oakland Center, increased route flexibility and reduced separation standards can potentially now be accommodated, which can translate directly into increased revenue for the airlines.

The characterization of the traffic patterns on the CEP routes was accomplished by first operating NASA's FACET in playback mode with 120 hrs. of the FAA's ASDI data from December 14-16 and 19-20. From this data set, 911 east- and westbound flights were identified that utilized at least one of the seven CEP routes. Using a suite of newly developed analysis capabilities, the following metrics were calculated: flight level usage, temporal flight distribution, CEP route usage, and origin-destination distribution.

Following the characterization of the nominal traffic patterns on the CEP routes, the results of a comprehensive investigation of the potential benefits associated with transitioning from the fixed CEP based routes to user-preferred routes were presented. To accomplish this task, the aforementioned wind-optimal dynamic programming algorithm was implemented in FACET, and 15, 24-hour simulations were conducted with the modified system. Of these simulations, five routed flights on the nominal (CEP-based) routes, five routed flights between the origin and destination on wind-optimal trajectories (OD), and the remaining five routed flights on nominal trajectories in the non-oceanic domain and wind-optimal trajectories in the oceanic domain (OCB).

The results of these 15, 24-hour simulations were characterized in terms sector count deviations, first loss of separation events, time savings, and distance savings. In general, only minor differences were found when comparing the nominal sector counts with the counts resulting from the wind-optimal simulations. This is significant, since the number of aircraft in a sector contributes significantly to the workload of a controller. In contrast, the number of simulated first-loss-of-separation events was found to dramatically increase in the wind-optimal simulations. To reduce the number of these events to an acceptable level, research into additional control strategies, such as departure control, should be investigated. Finally, the average time savings for the OD and OCB wind-optimal routing simulations was found to be 9.9 min and 4.8 min, respectively, while the average distance savings was found to be 36 nmi and 4.0 nmi, respectively.

In conclusion, wind-optimal routes offer a clear advantage over nominal (CEP-based) routes for the airspace users in the Central East Pacific, and research into new control strategies is essential for alleviating workload issues associated with this alternative routing strategy.

Appendix

For the current study, the incremental cost associated with transitioning between two successive states, x_k , and x_{k+1} , is equal to the travel time between these two states. If the initial latitude/longitude position is denoted by (λ_i, τ_i) and the final position is denoted by (λ_f, τ_f) then the cost/travel time is given by²⁰

$$C(x_k, u_k, k) = t = d / V_g \quad (15)$$

where

$$d = R_{earth} \cdot \cos^{-1} \left[\sin \lambda_i \cdot \sin \lambda_f + \cos(\tau_f - \tau_i) \cdot \cos \lambda_i \cdot \cos \lambda_f \right] \quad (16)$$

and

$$V_g = \sqrt{\dot{x}^2 + \dot{y}^2} \quad (17)$$

Here R_{earth} is the radius of the Earth, which is taken to be 3,444.046647 nm, and the horizontal components of the velocity are denoted by \dot{x} and \dot{y} . These velocity components are calculated from the horizontal velocity of the aircraft, v_h , the horizontal component of the wind velocity, w_h , the aircraft's commanded heading, χ_{com} , and the horizontal wind direction, χ_h , using the following expressions:

$$\dot{x} = v_h \cdot \cos \chi_{com} + w_h \cdot \cos \chi_h \quad (18)$$

and

$$\dot{y} = v_h \cdot \sin \chi_{com} - w_h \cdot \sin \chi_h \quad (19)$$

The aircraft's command heading, χ_{com} , is related the course angle for great circle navigation, χ_{GC} , via the following expression:

$$\chi_{com} = \chi_{GC} - \sin^{-1} \left((w_h / v_h) \cdot \sin(\chi_h - \chi_{GC}) \right) \quad (20)$$

where

$$\chi_{GC} = \tan^{-1} \left[\frac{\sin(\tau_f - \tau_i) \cdot \cos \lambda_f}{\sin \lambda_f \cdot \cos \lambda_i - \sin \lambda_i \cdot \cos \lambda_f \cdot \cos(\lambda_f - \lambda_i)} \right] \quad (21)$$

Acknowledgments

The authors would like to acknowledge the help of Mr. Kevin Chamness and Mr. David M. Maynard from the Federal Aviation Administration for providing the oceanic domain knowledge expertise required to complete this study. The assistance of Dr. Parimal Kopardekar from NASA Ames Research Center and Mrs. Almira Williams from CSSC, Inc. is also acknowledged for contributing to our understanding of flight routing and air traffic procedures in the Pacific Ocean.

References

¹Wu, Y. S., Karakis, T., and Merkle, M., "Performance Metrics for Oceanic Air Traffic Management," *Air Traffic Control Quarterly*, Vol. 12, No. 4, 2004, pp. 315-338.

²"Air Traffic Control," Order 7110.65R, Federal Aviation Administration, Feb. 16, 2006.

- ³“Advanced Technologies & Oceanic Procedures (ATOP),” U.S. Dept. of Transportation, Federal Aviation Administration, URL: http://www.faa.gov/airports_airtraffic/technology/atop
- ⁴Nolan, M., *Fundamentals of Air Traffic Control*, 4th ed., Thomson Brooks/Cole, Belmont, CA, pp. 467-470
- ⁵“Notice of Required Navigation Performance 10 (RNP-10) Implementation in the Oakland Center FIR,” Oakland NOTAM A4335/98, Federal Aviation Administration, 1998.
- ⁶Erzberger, H. and Lee, H., “Constrained Optimum Trajectories with Specified Range,” *AIAA Journal of Guidance, Navigation and Control*, Vol. 3, Jan-Feb, 1980, pp. 78-85.
- ⁷Jardin, M., “Real-Time Conflict Free Trajectory Optimization,” *5th USA/Europe ATM 2003 R&D Seminar*, Budapest, Hungary, June 23-27, 2005.
- ⁸Bertsimas, D. and Patterson, S. S., “The Traffic Flow Management Rerouting Problem in Air Traffic Control: A Dynamic Network Flow Approach,” *Transportation Science*, Vol. 34, No. 3, August 2000.
- ⁹Barnhart, C., Boland, N. L., Clarke, L. W., Johnson, G. L., Nemhauser, and G. L., Sheno, R. G., “Flight String Models for Aircraft Fleeting and Routing,” *Transportation Sciences*, Vol. 32, Issue 3, March 1998.
- ¹⁰Jardin, M., “Toward Real-Time En Route Air Traffic Control Optimization,” Ph.D. Dissertation, Stanford University, Dept. of Aeronautics & Astronautics, April 2003.
- ¹¹Larson, R. E. and Casti, J. L., *Principles of Dynamic Programming: Part 1 Basic Analytic and Computational Methods*, Marcel Dekker, Inc., 1978.
- ¹²Williams, E., “Aviation Formulary, V1.42,” URL: <http://williams.best.vwh.net/avform.htm>.
- ¹³“Enhanced Traffic Management System (ETMS),” Report No. VNTSC-DTS56-TMS-002, Volpe National Transportation Center, U.S. Dept. of Transportation, Cambridge, MA, Oct. 2005.
- ¹⁴“Aircraft Situation Display To Industry: Functional Description and Interface Control Document,” Report No. ASDI-FD-001, Volpe National Transportation Center, U.S. Dept. of Transportation, Cambridge, MA, June 29, 2005.
- ¹⁵Bilimoria, K., Sridhar, B., Chatterji, G. B., Sheth, K., and Grabbe, S., “FACET: Future ATM Concepts Evaluation Tool,” *Air Traffic Control Quarterly*, Vol. 9, No. 1, 2001, pp. 1-20.
- ¹⁶“EMC Model Documentation,” National Centers for Environmental Predictions, National Oceanic and Atmospheric Administration, URL: <http://www.emc.ncep.noaa.gov/modelinfo/>.
- ¹⁷Ahrens, C. D., *Essentials of Meteorology: An Invitation to the Atmosphere*, West Publishing Company, St. Paul, MN, 1993, pp. 177-179.
- ¹⁸Bertsimas, D., and Patterson S. S., “The Air Traffic Flow Management Problem with Enroute Capacities,” *Operations Research*, Vol. 46, No. 3, May-June 1998, pp. 406-422.
- ¹⁹Sridhar, B., Sheth, K. S., Grabbe, S., “Airspace Complexity and its Application in Air Traffic Management,” *2nd USA/Europe Air Traffic Management R&D Seminar*, Orlando, FL, Dec. 1-4, 1998.
- ²⁰Chatterji, G. B., Sridhar, B., and Bilimoria, K. D., “En-route Trajectory Prediction for Conflict Avoidance and Traffic Management,” *AIAA Guidance Navigation and Control Conference*, San Diego, CA, July 29-31, 1996.